Poro-mechanical analysis of a biomimetic scaffold for osteochondral defects

(Article begins on next page)

24 April 2024

PORO-MECHANICAL ANALYSIS OF A BIOMIMETIC SCAFFOLD FOR OSTEOCHONDRAL DEFECTS

Pietro Mascheroni[1], **Alfio Grillo**[2], **and Daniela P. Boso**[3]

[1] Department of Systems Immunology, Helmholtz Centre for Infection Research
Inhoffenstraße 7, D-38124, Braunschweig, Germany
e-mail: pietro.mascheroni@helmholtz-hzi.de

[2] Dipartimento di Scienze Matematiche "G.L. Lagranage", "Dipartimento di Eccellenza 2018-2002",
Politecnico di Torino
Corso Duca degli Abruzzi 24, I-10129, Torino, Italy
alfio.grillo @polito.it

[3] Department of Civil, Environmental and Architectural Engineering, University of Padova
Via F. Marzolo 9, I-35131, Padova, Italy
daniela.boso@unipd.it

Keywords: Osteochondral defects, Tissue engineering, Biomimetic scaffolds, Porous media mechanics, Finite Element Analysis.

Abstract. *Osteochondral defects are focal areas of damage involving articular cartilage and sub-chondral bone. Tissue engineering scaffolds are used to improve the organism regeneration ability for this kind of injury, serving as biocompatible structures for cell viability and differentiation. Since biomechanical cues such as substrate stiffness, loading conditions and fluid permeation are fundamental for successful tissue repair, understanding how these features vary in the scaffold is of primary importance. Here we present a mathematical model based on porous media mechanics for the analysis of a tissue engineering scaffold. We consider a three-layered scaffold mimicking a complete osteochondral tissue and vary the mechanical properties of the intermediate layer over a physiological range. Our results show that the interstitial fluid pressure and the vertical component of the solid effective stress depend significantly on the stiffness and permeability of the intermediate layer under mechanical loading. By properly tuning these material properties, regimes of slow or fast temporal variations of mechanical stress can be obtained in the scaffold layer of interest.*

1 INTRODUCTION

Osteochondral defects are deficiencies that involve both the articular cartilage and the subchondral bone underneath. While articular cartilage has poor healing capabilities, osteochondral injuries reveal a better attitude for spontaneous repair thanks to the mesenchymal stem cells (MSCs) that can reach the defect from the nearby bone marrow. MSCs can differentiate and synthetize new bone and cartilage tissues. However, this natural reparative ability gives rise to the formation of tissue layers that are biomechanically inferior and demonstrate to degrade over time with extensive fissuring and fibrillations [1]. Tissue engineering (TE) of osteochondral composites can offer a possible solution to this limit. Scientific advances in our knowledge of biomaterials, stem cells, growth and differentiation factors, and the fast improvement in bioreactor technology offer great opportunities to fabricate tissues in the laboratory from combinations of engineered extracellular matrices (scaffolds), cells, and biologically active molecules. Healing and regeneration of osteochondral defects are not trivial, as the process requires an avascular collagen deposition on the cartilage region concurrently with a vascular calcification in the bone stratum. TE scaffolds provide a suitable frame for cell attachment and differentiation, offering segregated skeletons for the various cell populations requiring different biochemical and biomechanical environments. Up to now, several approaches have been proposed for the fabrication of osteochondral composites, revealing that the regeneration process and its requirements are not fully understood yet. Experimental studies [2] have shown that several factors influence the quality and durability of the repair tissue, such as the type of scaffold [3], *in vitro* cultivation time [4], cell sources [5], [6], and type of loading [7]–[11]. Merely experimental approaches to define the effects of the various factors can be very expensive in time and money, and sometimes would not provide a full understanding of the process. To fill this gap, mathematical modelling and computational simulation can be very useful, as they allow an easy manipulation of the parameters and a high number of tests at no practical cost and, furthermore, can guide the preparation of real experimental tests. In this paper, we present a model based on porous media mechanics for the analysis of a biomimetic scaffold for the treatment of osteochondral defects. In the following, we consider a three-layer scaffold mimicking a complete osteochondral tissue, composed of the articular cartilage layer, the subchondral bone layer and a calcified cartilage interface (tidemark) between the two distinct regions.

2 MATHEMATICAL MODEL

We derive the mathematical model of the tissue scaffold from the work in [12]–[15], considering the scaffold as a biphasic porous material. Here, we restrict our study to the simplest case of isotropic porous medium. We are aware, however, that transversely isotropic models of articular cartilage have been proposed e.g. in [14], [15] (see also the references therein). Although an anisotropic description of the tissue scaffold is more realistic, we prefer to consider only an isotropic model, because we should otherwise distinguish between the anisotropy of the cartilage from that of the tidemark and of the bone. A model capable of capturing these details is part of our current studies. The following equations are formulated for each of the scaffold subdomains, i.e. cartilage (C), tidemark (T) and bone (B). Neglecting growth and mass exchange processes, the mass and linear momentum balance laws for the α-th phase are given by:

$$\partial_t(\varepsilon_\alpha \rho_\alpha) + \mathrm{div}(\varepsilon_\alpha \rho_\alpha \boldsymbol{v}_\alpha) = 0, \tag{1}$$

$$\mathrm{div}\,\boldsymbol{\sigma}_\alpha + \boldsymbol{m}_\alpha = 0, \tag{2}$$

$$\boldsymbol{m}_{\mathrm{s}} + \boldsymbol{m}_{\mathrm{f}} = 0, \tag{3}$$

with α=s, f for the solid and fluid phase, respectively. In (1)-(3), ε_α is the volumetric fraction, ρ_α is the mass density, $\boldsymbol{v}_\alpha$ is the velocity, $\boldsymbol{\sigma}_\alpha$ is Cauchy stress tensor, and $\boldsymbol{m}_\alpha$ is the internal force density that the α-th constituent exchanges with the other one. Furthermore, we require the saturation condition

$$\varepsilon_{\mathrm{s}} + \varepsilon_{\mathrm{f}} = 1. \tag{4}$$

Note that, by summing (2) over the two phases and applying the closure condition in (3), it is possible to write the balance of linear momentum for the whole mixture as:

$$\mathrm{div}(\boldsymbol{\sigma}_{\mathrm{s}} + \boldsymbol{\sigma}_{\mathrm{f}}) = 0. \tag{5}$$

Then, we regard the fluid phase as macroscopically inviscid and we assume the constituents to be incompressible. In this way, the stress tensors of the solid and the fluid phase can be expressed as:

$$\boldsymbol{\sigma}_{\mathrm{s}} = -\varepsilon_{\mathrm{s}} p_{\mathrm{f}} \boldsymbol{I} + \boldsymbol{\sigma}_{\mathrm{s}}^{\mathrm{eff}}, \tag{6}$$
$$\boldsymbol{\sigma}_{\mathrm{f}} = -\varepsilon_{\mathrm{f}} p_{\mathrm{f}} \boldsymbol{I}, \tag{7}$$

in which $\boldsymbol{I}$ is the identity tensor, p_{f} represents the fluid pressure, and $\boldsymbol{\sigma}_{\mathrm{s}}^{\mathrm{eff}}$ is referred to as the effective Cauchy stress tensor of the solid phase. The latter quantity is determined as

$$\boldsymbol{\sigma}_{\mathrm{s}}^{\mathrm{eff}} = \frac{1}{J} \boldsymbol{F} \left(2 \frac{\partial W}{\partial \boldsymbol{C}} \right) \boldsymbol{F}^{T} \tag{8}$$

with J being the determinant of the deformation gradient tensor, $\boldsymbol{F}$, W the strain energy density of the solid phase, and $\boldsymbol{C}$ the right Cauchy-Green deformation tensor. In the following, we choose the Holmes-Mow strain-energy density [16], i.e.

$$W = a_0 [\exp(\psi) - 1], \quad \psi = a_1 (I_1 - 3) + a_2 (I_2 - 3) - \beta \ln(I_3), \tag{9}$$

where I_1, I_2 and I_3 are the invariants of $\boldsymbol{C}$ and a_0, a_1, a_2 and β are coefficients related to material properties by the relations [14]:

$$a_0 = \frac{2\mu + \lambda}{4\beta}, \quad a_1 = \beta \frac{2\mu - \lambda}{2\mu + \lambda}, \quad a_2 = \beta \frac{\lambda}{2\mu + \lambda}, \quad \beta = a_1 + 2a_2,$$

in which λ and μ are the Lamé constants of the respective scaffold layer. Note that, by substituting (6) and (7) in (5), it is possible to write the linear momentum balance for the biphasic system in terms of the effective Cauchy stress:

$$\mathrm{div}\left(\boldsymbol{\sigma}_{\mathrm{s}}^{\mathrm{eff}} - p_{\mathrm{f}} \boldsymbol{I} \right) = 0. \tag{10}$$

Regarding the fluid problem, summing (1) over the two phases yields

$$\mathrm{div}(\boldsymbol{q}) + \mathrm{div}(\boldsymbol{v}_{\mathrm{s}}) = 0, \tag{11}$$

where $q = \varepsilon_f(v_f - v_s)$. We assume that the standard assumptions leading to Darcy's law are valid [17], [18], and we write:

$$q = -k\,\text{grad}\,p_f \tag{12}$$

where k is the hydraulic conductivity tensor of the system. Note that if, in the terminology of Ateshian and Weiss [19], the hydraulic response of the biphasic mixture is "unconditionally isotropic", k can be expressed as a function of the third invariant of C, i.e., $k = k_0(J)I$. Following [13], [16], we assume for k_0 the relation:

$$k_0(J) = k_r \left(\frac{J - \varepsilon_s^0}{1 - \varepsilon_s^0}\right)^{m_0} \exp\left[\frac{m_1}{2}(J^2 - 1)\right], \tag{13}$$

where k_r is the reference hydraulic conductivity of the material, m_0 and m_1 are material parameters and ε_s^0 is the volume fraction of the solid phase in the reference configuration. To complete the mathematical model, we recall that the sets of equations are accompanied by the following interface conditions, which apply at the internal boundaries separating the three subdomains C, T, B:

$$[\![v_s \cdot n]\!]_{I_{\gamma\delta}} = 0, \tag{14}$$

$$[\![\varepsilon_f v_f \cdot n]\!]_{I_{\gamma\delta}} = 0, \tag{15}$$

$$[\![(\sigma_s + \sigma_f)\,n]\!]_{I_{\gamma\delta}} = 0, \tag{16}$$

$$[\![p_f]\!]_{I_{\gamma\delta}} = 0. \tag{17}$$

Here, the symbol $[\![\cdot]\!]$ represents the jump at the interface $I_{\gamma\delta}$ for its argument (γ, δ = C, T, B) and n is the unit vector normal to $I_{\gamma\delta}$.

Figure 1A displays a schematic of the scaffold and its positioning in the body, together with the disposition of the three layers. Since the scaffold has a cylindrical structure, we enforce axial symmetry in the following. The scaffold geometry is represented in Figure 1B, with the unit expressed in millimeters. The layers have a similar height, with the tidemark possessing the smallest value. Figure 1C represents the boundary conditions applied at the scaffold surface during the analysis. We enforce no fluxes at the top and bottom surface, whereas impose zero fluid pressure on the lateral surface. In addition, we impose zero vertical displacements on the top surface and a boundary force on the bottom one. The remaining surface is left free to deform. We consider a time dependent loading of the scaffold, as shown in Figure 1D. The maximum vertical load is linearly ramped over time from 0 to 1 seconds; then, the load is kept constant until 6 seconds and finally linearly reduced to zero at 7 seconds. Figure 1E shows the points in the scaffold in which we evaluate the model observables during the simulation. We select two points for each layer, one at the center and the other close to the lateral surface of the scaffold. The properties of the materials constituting the scaffold layers are summarized in Table 1. We vary the properties of the tidemark over a wide range and report the results of the analysis in the Results section.
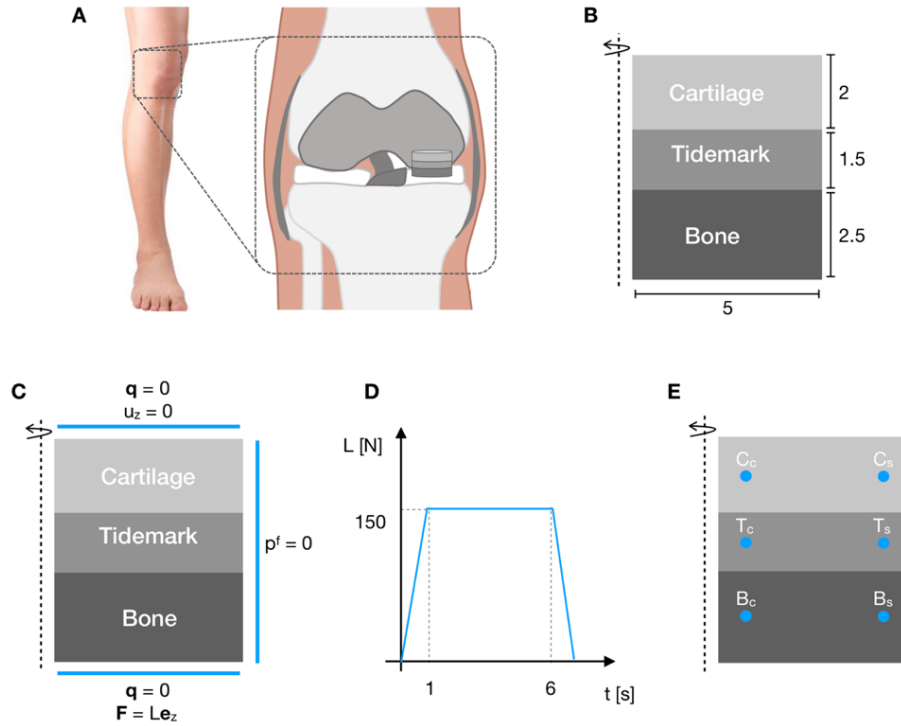
Figure 1: **A** Schematic of the three-layered scaffold and positioning in the body (image adapted from [20]). **B** Scaffold geometry, with lengths expressed in mm. **C** Boundary conditions of the Finite Element problem. **D** Time dependence of the boundary load applied at the bottom surface of the scaffold. **E** Points in the scaffold in which the model observables are evaluated over time.

Parameter	Value	Description	Reference
λ_c	2.02 [MPa]	Cartilage Lamé's first parameter	[9]
μ_c	4.31 [MPa]	Cartilage Lamé's second parameter	[9]
λ_t	$(0.03, 0.34, 3.46) \times 10^3$ [MPa]	Tidemark Lamé's first parameter	Model specific
μ_t	$(0.04, 0.4, 4.06) \times 10^3$ [MPa]	Tidemark Lamé's second parameter	Model specific
λ_b	9.51×10^3 [MPa]	Bone Lamé's first parameter	[9]
μ_b	6.34×10^3 [MPa]	Bone Lamé's second parameter	[9]
k_{rc}	5×10^{-15} [m⁴/(Ns)]	Cartilage reference hydraulic conductivity	[9]
k_{rt}	$(0.01, 0.1, 1) \times 10^{-15}$ [m⁴/(Ns)]	Tidemark reference hydraulic conductivity	Model specific
k_{rb}	1×10^{-17} [m⁴/(Ns)]	Bone reference hydraulic conductivity	[9]
ε_s^0	0.2	Initial solid volume fraction	Model specific
m_0	8.48×10^{-2}	Parameter for the hydraulic conductivity	[16]
m_1	4.63	Parameter for the hydraulic conductivity	[16]
L	150 [N]	Vertical loading force	Model specific

Table 1: Summary of the parameters used in the model.

3   RESULTS

Figure 2 shows the contour plots of the Interstitial Fluid Pressure (IFP) p_f and the Vertical Effective Stress (VES) σ_z^{eff} at different time points during the simulation. We used an intermediate value for the tidemark stiffness and permeability, keeping the other parameters as in Table 1. During the loading phase ($0 < t < 1s$) the IFP decreases in the region of the bone close to the tidemark layer, whereas it increases close to the bone bottom surface (Figure 2A). The pressure difference relaxes over time, until it changes sign in the unloading phase. The tidemark layer, on the other hand, withstands a pressure increase over time, as the interstitial fluid flows downwards from the cartilage. The latter layer is the most compliant and experiences a steady increase in IFP during the loading phase. Figure 2B shows model results for the vertical component of the effective stress. Note that solid stress and interstitial pressure have opposite signs for compression, as customary in porous media literature. The increase of IFP during loading leads to tensile stresses at the bottom of the bone layer, which relax and change sign towards the end of the simulation. The opposite occurs in the region of the bone close to the tidemark layer, where initial compression of the solid component is followed by tension in the unloading stage. The situation is similar for the other layers, where the VES mirrors the IFP response over time.

We performed a parametric analysis by varying the tidemark stiffness and hydraulic conductivity over a wide range. Results for IPF and VES are reported in Figures 3 and 4 at the different observation points defined in Figure 1E. We used red, blue and green to identify different degrees of solid skeleton stiffness (red: low, blue: intermediate, green: high) whereas a gradient of color hue is used to represent increasing hydraulic conductivity (darker colors for
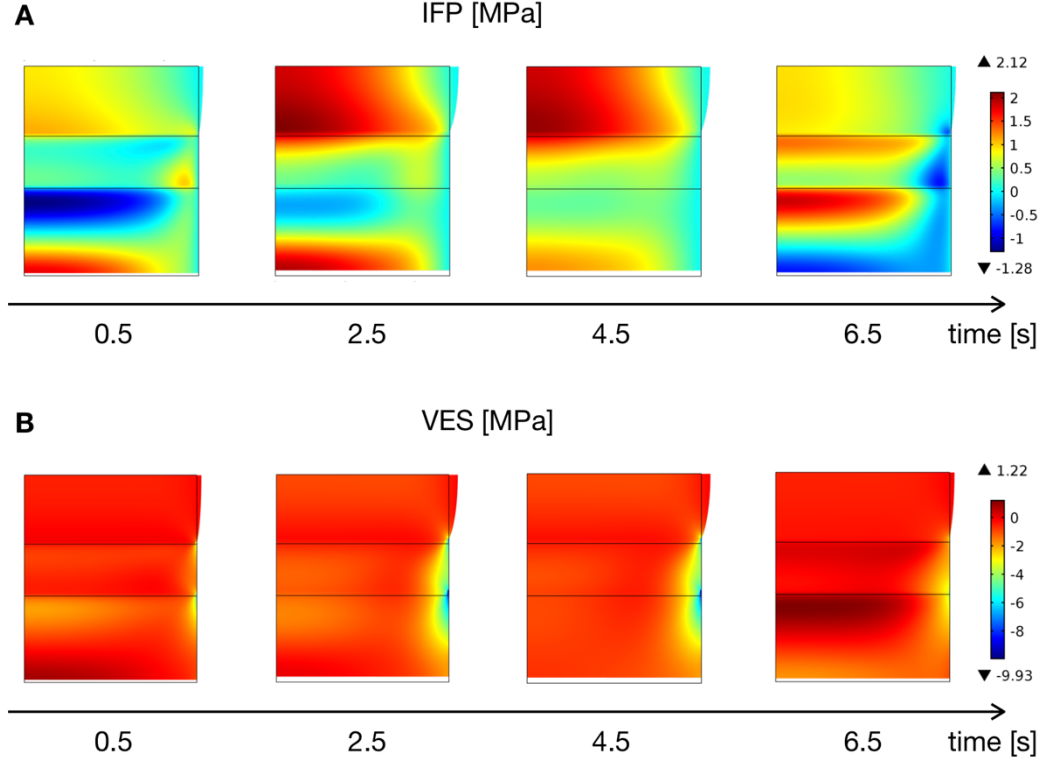

Figure 2: Contour plots of IFP and VES at different time points in the simulation. We used the values $\lambda_t = 3.46 \times 10^2$ MPa, $\mu_t = 4.06 \times 10^2$ MPa, $k_{rt} = 10^{-16}$ [m^4/(Ns)]. The other parameters are as in Table 1.

higher hydraulic conductivity values). Figure 3A and 3B show that the properties of the tidemark layer do not influence significantly the IFP in the cartilage layer in the central and side points of the scaffold. On the other hand, profound changes are visible in the tidemark layer itself. Figure 3C displays similar IFPs for low stiffness and low and intermediate hydraulic conductivities. On the contrary, the IFP increases with increasing hydraulic conductivity for increasing stiffness of the layer. The opposite behavior occurs in the side point, displayed in Figure 3D. As the layer becomes more permeable, the fluid flows faster out of the scaffold and the IFP is reduced. Figures 3E and 3F show the IFP response for the bone layer. Low tidemark stiffness leads to negative pressures in the pores in the loading stage, which turn positive at later times. The comparatively high stiffness of the tidemark, on the other hand, increases the rigidity of the whole structure and contributes to higher IFPs from the beginning of the loading. Figure 3F shows that close to the scaffold free surface the IFP in the bone layer does not depend significantly on the properties of the tidemark.

Figure 4 shows the results of the analysis in terms of VES. Also in this case, Figure 4A and 4B display that the stress in the cartilage depends weakly on the properties of the tidemark layer. Figure 4C on the other hand reveals significant variation in the stress for the different material parameters. The VES decreases with increasing stiffness of the intermediate scaffold layer and for decreasing hydraulic conductivities. This is particularly true in the central region of the scaffold, whereas the stresses close to the scaffold free surface range between -2 and -1 MPa (Figure 4D). In a similar way, the stresses in the bone do not depart too much from one another, both in the center and side of the scaffold as shown in Figures 4E and 4F.

4. CONCLUSIONS

We presented a parametric study analyzing the impact of poromechanics on a biomimetic scaffold designed for the treatment of osteochondral defects. We tested the effects of different material properties of the intermediate layer of the scaffold (tidemark) on the interstitial fluid pressure and vertical effective stress in several scaffold points. Our results demonstrate that, by changing the stiffness and hydraulic conductivity of the tidemark, the pressure and stress profiles change significantly both in the tidemark itself and in the bone layer. On the contrary, the two observables depend only weakly on the tidemark properties in the cartilage layer, both in the central and lateral part of the scaffold. The analysis also shows that small variations of fluid pressure and vertical effective stress in the bone (center and side) can be obtained for high stiffness and low hydraulic permeability of the tidemark. On the other hand, large variations in pressure and stress are possible for low and intermediate tidemark stiffness for all the analyzed hydraulic conductivity levels.
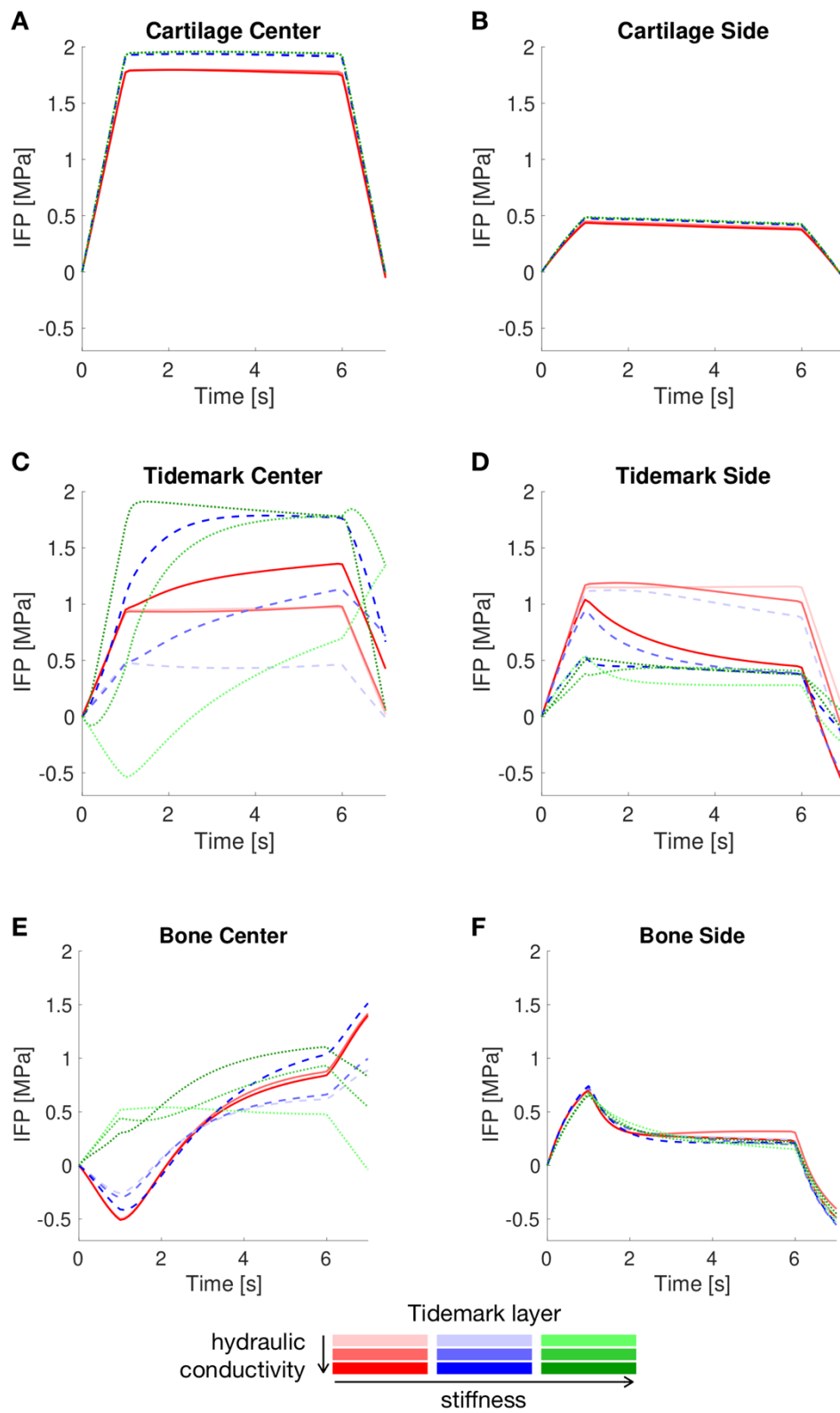
Figure 3: IFP variation over time at the observation points defined in Figure 1E. A, C, E refer to points at the center of the scaffold, whereas B, D, F to points close to the scaffold free surface. The color legend is as follows: red, blue and green lines are used for increasing tidemark stiffness, respectively. In addition, darker color hues are used to denote increasing hydraulic conductivity of the tidemark layer.

Figure 4: VES variation over time at the observation points defined in Figure 1E. A, C, E refer to points at the center of the scaffold, whereas B, D, F to points close to the scaffold free surface. The color legend is as follows: red, blue and green lines are used for increasing tidemark stiffness, respectively. In addition, darker color hues are used to denote increasing hydraulic conductivity of the tidemark layer.
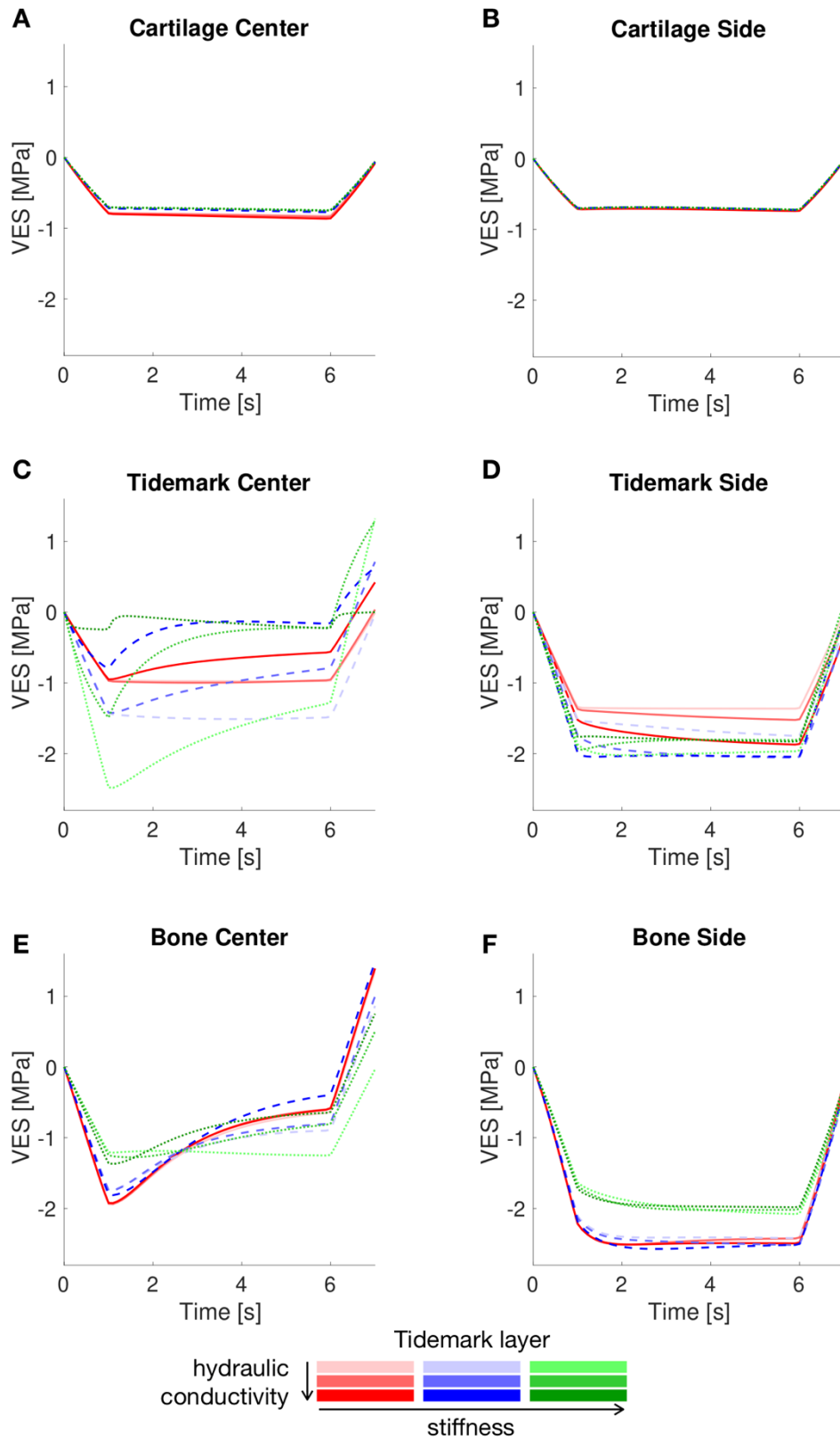
REFERENCES

[1]   F. Shapiro, S. Koide, M. J. Glimcher, Cell origin and differentiation in the repair of full-thickness defects of articular cartilage. *The Journal of Bone & Joint Surgery*, **75**, 532–553, 1993.

[2]   I. Martin, S. Miot, A. Barbero, M. Jakob, D. Wendt, Osteochondral tissue engineering. *Journal of Biomechanics*, **40**, 750–765, 2007.

[3]   C.-H. Chang, F.-H. Lin, C.-C. Lin, C.-H. Chou, H.-C. Liu, Cartilage tissue engineering on the surface of a novel gelatin-calcium-phosphate biphasic scaffold in a double-chamber bioreactor. *Journal of Biomedical Materials Research*, **71B**, 313–321, 2004.

[4]   D. Schaefer, I. Martin, P. Shastri, R. . Padera, R. Langer, L. . Freed, G. Vunjak-Novakovic, In vitro generation of osteochondral composites. *Biomaterials*, **21**, 2599–2606, 2000.

[5]   P. Benya, J. D. Shaffer, Dedifferentiated chondrocytes reexpress the differentiated collagen phenotype when cultured in agarose gels. *Cell*, **30**, 215–224, 1982.

[6]   F. Binette, D. P. McQuaid, D. R. Haudenschild, P. C. Yaeger, J. M. McPherson, R. Tubo, Expression of a stable articular cartilage phenotype without evidence of hypertrophy by adult human articular chondrocytesin vitro. *Journal of Orthopaedic Research*, **16**, 207–216, 1998.

[7]   D. J. Kelly, P. J. Prendergast, Mechano-regulation of stem cell differentiation and tissue regeneration in osteochondral defects. *Journal of biomechanics*, **38**, 1413–22, 2005.

[8]   D. R. Carter, P. R. Blenman, G. S. Beaupré, Correlations between mechanical stress history and tissue differentiation in initial fracture healing. *Journal of Orthopaedic Research*, **6**, 736–748, 1988.

[9]   D. Lacroix, P. J. Prendergast, A mechano-regulation model for tissue differentiation during fracture healing: analysis of gap size and loading. *Journal of biomechanics*, **35**, 1163–71, 2002.

[10]   G. N. Duda, Z. M. Maldonado, P. Klein, M. O. W. Heller, J. Burns, H. Bail, On the influence of mechanical conditions in osteochondral defect healing. *Journal of Biomechanics*, **38**, 843–851, 2005.

[11]   T.-A. N. Kelly, K. W. Ng, C. C.-B. Wang, G. A. Ateshian, C. T. Hung, Spatial and temporal development of chondrocyte-seeded agarose constructs in free-swelling and dynamically loaded cultures. *Journal of Biomechanics*, **39**, 1489–1497, 2006.

[12]   P. Mascheroni, M. Carfagna, A. Grillo, D. P. Boso, B. A. Schrefler, An avascular tumor growth model based on porous media mechanics and evolving natural states. *Mathematics and Mechanics of Solids*, **23**, 686–712, 2018.

[13]   A. Grillo, R. Prohl, G. Wittum, A poroplastic model of structural reorganisation in porous media of biomechanical interest. *Continuum Mechanics and Thermodynamics*, **28**, 579–601, 2016.

[14]   A. Tomic, A. Grillo, S. Federico, Poroelastic materials reinforced by statistically oriented fibres--numerical implementation and application to articular cartilage. *IMA Journal of Applied Mathematics*, **79**, 1027–1059, 2014.

[15]   S. Federico, A. Grillo, Elasticity and permeability of porous fibre-reinforced materials under large deformations. *Mechanics of Materials*, **44**, 58–71, 2012.

[16]   M. H. Holmes, V. C. Mow, The nonlinear characteristics of soft gels and hydrated connective tissues in ultrafiltration. *Journal of Biomechanics*, **23**, 1145–1156, 1990.

[17]   J. Bear, *Dynamics of fluids in porous media*. Courier Corporation, 2013.

[18]   S. Majid Hassanizadeh, Derivation of basic equations of mass transport in porous

media, Part 2. Generalized Darcy's and Fick's laws. *Advances in Water Resources*, **9**, 207–222, 1986.

[19] G. A. Ateshian, J. A. Weiss, Anisotropic Hydraulic Permeability Under Finite Deformation. *Journal of Biomechanical Engineering*, **132**, 111004, 2010.

[20] M. Pizzocaro, Modelling biomechanical problems in the framework of porous media mechanics: diabetic foot and biologically inspired scaffolds. 2016.